

Effects of *A*-site ordering on the Mn local structure and polar phases of $R\text{BaMn}_2\text{O}_6$ ($R = \text{La, Nd, Sm, and Y}$)

G. Subías ^{1,2,*}, J. Blasco,^{1,2} V. Cuartero ^{1,3}, S. Lafuerza,^{1,2} L. Simonelli,⁴ G. Gorni ^{4,5}, M. Castro ^{1,3} and J. García^{1,2}

¹*Instituto de Nanociencia y Materiales de Aragón (INMA), CSIC-Universidad de Zaragoza, 50009 Zaragoza, Spain*

²*Departamento de Física de la Materia Condensada, Universidad de Zaragoza, C/ Pedro Cerbuna 12, 50009 Zaragoza, Spain*

³*Departamento de Ciencia y Tecnología de Materiales y Fluidos, EINA, Universidad de Zaragoza, C/ María de Luna 3, 50018, Zaragoza, Spain*

⁴*CELLS-ALBA Synchrotron Light Source, 08290 Cerdanyola del Vallès, Barcelona, Spain*

⁵*Instituto de Óptica (IO-CSIC), C/ Serrano, 121, 28006 Madrid, Spain*



(Received 24 May 2022; revised 31 January 2023; accepted 27 March 2023; published 19 April 2023)

We have investigated the temperature dependence of the Mn local structure in *A*-site ordered $R\text{BaMn}_2\text{O}_6$ ($R = \text{La, Nd, Sm, and Y}$) perovskites, in parallel with their disordered counterparts, $R_{0.5}\text{Ba}_{0.5}\text{MnO}_3$, by means of x-ray emission (XES) and x-ray absorption spectroscopy (XAS). The end member $\text{LaBaMn}_2\text{O}_6$ shows a nearly regular MnO_6 octahedron independent of temperature. With decreasing the R ionic radius in the ordered samples, the XAS results indicate that a local distortion develops in the MnO_6 octahedron at the low-temperature charge-localized and polar phases. For $\text{NdBaMn}_2\text{O}_6$, this local distortion is tiny, indicating the absence of charge segregation at the Mn site. This is followed by a bigger local distortion anticipated for $\text{SmBaMn}_2\text{O}_6$ in its respective charge-localized and polar phase and finally, the biggest local distortion for the smallest *A*-site cation ordered compound, YBaMn_2O_6 , for which it even persists above the polar charge-localization transition temperatures. The high-resolution XAS spectra confirm the presence of charge segregation between two nonequivalent Mn sites in the low-temperature polar phase of Sm and Y ordered samples. Thus, our XAS study suggests a displacive mechanism for the charge-localization and polar transitions in the Nd and Sm ordered samples while a combination of displacive and order-disorder contributions is revealed for YBaMn_2O_6 . Besides, calorimetric measurements confirm the combination of the two mechanisms, order-disorder and displacive, for the ordered Sm and Y compounds. On the other hand, the *A*-site disordered $R_{0.5}\text{Ba}_{0.5}\text{MnO}_3$ samples with R cations smaller than Nd present a significant static (temperature-independent) local disorder, which explains why polar charge-localization transitions are not developed in these samples. Finally, we correlate our results about the Mn local structure and character of the transitions with the macroscopic magnetic and electric behavior of both *A*-site ordered and disordered compounds.

DOI: [10.1103/PhysRevB.107.165133](https://doi.org/10.1103/PhysRevB.107.165133)

I. INTRODUCTION

Perovskite-type manganese oxides $R_{1-x}D_x\text{MnO}_3$ ($R =$ trivalent rare earth, $D =$ divalent cation) have focused widespread interest in the last decades thanks to the key discovery of their colossal magnetoresistance behavior [1]. However, the physical properties exhibited by manganites are not limited to this phenomenon, and also include, for instance, metal-insulator transitions, thermoelectricity, ferroelectricity, and (anti)ferromagnetism [2–7]. The latter two types of orderings may appear simultaneously and be coupled in magnetoelectric multiferroics [6,7]. The magnetoelectric properties in $R_{1-x}D_x\text{MnO}_3$ arises from the interplay between the structural (lattice), electronic (orbital and charge), and magnetic (spin) instabilities depending on the combination of the R and D elements. In general, R and DE randomly occupy the *A* sites in the perovskite-type ABO_3 structure [Fig. 1(a)] causing this system to have inherent disorder in the lattice but when divalent D cation is Ba, the different ionic size favors the ordering of Ba and R atoms in the *A* site of the perovskite-type

lattice. In particular, for $x = 0.5$, i.e., $R\text{BaMn}_2\text{O}_6$ stoichiometry, R and Ba ions can alternately occupy the *A* sites along the *c* axis if the synthesis conditions are properly controlled [8,9] [Fig. 1(b)]. The structure of *A*-site ordered double-perovskites $R\text{BaMn}_2\text{O}_6$ ($R =$ rare earth, Y) comprises a MnO_2 square sublattice sandwiched between two types of rocksalt layers (RO and BaO) with strong size difference. Consequently, the strained MnO_6 octahedron is distorted in a peculiar manner with the Mn and O atoms of the MnO_2 plane shifted toward the RO layer for an ordered system. This can favor the appearance of polar phases in contrast with the apparent rigid octahedron observed in the disordered $R_{0.5}\text{Ba}_{0.5}\text{MnO}_3$ analogs [Fig. 1(a)]. Therefore, ordered $R\text{BaMn}_2\text{O}_6$ and disordered $R_{0.5}\text{Ba}_{0.5}\text{MnO}_3$ samples with the same stoichiometry can be studied to unveil the correlation between magnetoelectric properties and underlying crystallographic and local structures.

We have recently characterized the ordered $R\text{BaMn}_2\text{O}_6$ ($R = \text{La, Pr, Nd, Sm, and Y}$) compounds with respect to their crystallographic structures and magnetoelectric properties as a function of the ionic radius of R atoms [see Fig. S1(a) in the Supplemental Material] [10–12]. In Table I we summarize the relevant structural, electric, and magnetic

*gloria@unizar.es

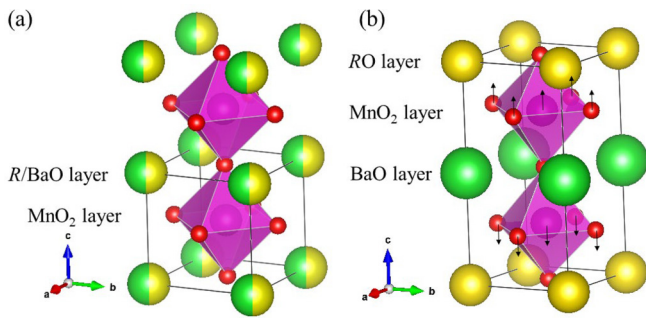


FIG. 1. Schematic representation of (a) the ideal cubic structure of A -site disordered $R_{0.5}\text{Ba}_{0.5}\text{MnO}_3$ perovskites and (b) the ideal tetragonal $P4/mmm$ crystal structure of A -site ordered RBaMn_2O_6 perovskites. Black arrows in (b) illustrate the displacement of the MnO_2 plane towards the RO layers in the RBaMn_2O_6 perovskites resulting in a distorted MnO_6 octahedron.

properties of the samples presented in this study as a function of the ratio of ionic radius $r_{R^{3+}}/r_{\text{Ba}^{2+}}$. For R elements with ionic radius larger than Sm, i.e., Nd, Pr, and La, ferromagnetic (FM) correlations are enhanced and the three ordered samples are isostructural at high temperature (440 K). They adopt the tetragonal structure of a perovskite with A -site ordering without tilts of the MnO_6 octahedron [10] (space group $P4/mmm$). $\text{LaBaMn}_2\text{O}_6$ undergoes a ferromagnetic (FM) phase transition with anisotropic changes in the tetragonal lattice parameters related to the orientation of the Mn-ordered moments. Ordered $\text{PrBaMn}_2\text{O}_6$ exhibit first a FM transition. Second, a further transition to an A -type layered antiferromagnetic (AFM) state with ferromagnetic planes coupled antiferromagnetically along the c axis takes place simultaneously to a structural metal-to-insulator transition. Ordered $\text{NdBaMn}_2\text{O}_6$ shows magnetic properties similar to $\text{PrBaMn}_2\text{O}_6$ but long-range FM order is not established in this compound. Instead, short-range FM correlations are present above the AFM transition. The low-temperature phase is polar for both $\text{PrBaMn}_2\text{O}_6$ and $\text{NdBaMn}_2\text{O}_6$ compounds but there is a single site for the Mn atom, incompatible with the occurrence of a significant charge segregation. Furthermore, the contribution from the asymmetric stretching associated with a Jahn-Teller distortion is found negligible in this structural transition, suggesting the lack of ferroic orbital ordering (OO). Interestingly, the A -site disorder in these La-, Pr-, and Nd-based manganites weakens the FM transition [Table I and see Fig. S1(b)] but also the A -type AFM transition to some extent [13].

For R elements with small ionic radius, such as Sm and Y, two successive structural phase transitions take place on cooling from 500 down to 100 K [Table I and see Fig. S1(a)], while resistivity measurements clearly show a first-order metal-insulator-like transition along with one of the structural transitions [11,14]. These transitions result in nonequivalent Mn sites with the presence of charge segregation between them. Since charge segregation between the nonequivalent Mn sites is clearly below the nominal value of one charge unit between Mn^{3+} and Mn^{4+} , we refer to them as charge-localization (CL) transitions. The main difference between the two structural phases concerns the stacking sequence of the ordered charge segregation along the c axis, which is

double for the high-temperature phase. The mismatch between the RO and BaO sublattices is the largest so the corresponding CL transition temperature, T_{CL} , increases with decreasing the R size well above room temperature for the first high-temperature transition (Table I) [11,12]. Moreover, the low-temperature CL phase displays a Jahn-Teller-like distortion for one of the nonequivalent Mn sites which has been generally ascribed to OO. In addition, this low-temperature CL phase has a polar symmetry that allows spontaneous ferroelectric polarization [11–15] and the magnetic ground state is characterized by CE-type AFM ordering, consisting of FM zigzag chains in the ab plane that are AFM coupled to each other and along the c axis. The simultaneous occurrence of ferroelectricity and magnetic ordering indicates that these compounds can be considered as type-II multiferroics [16] and might present magnetoelectric coupling. On the other hand, the corresponding polymorph compounds fully disordered in the A site, $R_{0.5}\text{Ba}_{0.5}\text{MnO}_3$ ($R = \text{Sm}$ and Y), do not exhibit either polar CL-like phases or long-range magnetic ordering [Table I and see Fig. S1(b)] [17,18].

Thus, it is noteworthy that the occurrence of polar phases and, consequently ferroelectricity, in these systems strongly depend on the size of the A -site rare-earth cation and the degree of A -site order, which can break the inversion symmetry at the Mn sites. While characterizing the Mn local structure of the different magnetoelectric phases is key to elucidate the mechanism driving the polar transitions, this information is very limited in the ordered systems. The ferroelectric mechanism is termed displacive when the structural distortions strictly vanish in the paraelectric phase, and order-disorder when they are nonvanishing but thermally average out to zero in the paraelectric phase [19]. The extended x-ray absorption fine-structure (EXAFS) technique is ideally suited for determination of the dynamic local structure around a specific absorbing atom due to the short interaction time ($\sim 10^{-15}$ s) of the photoabsorption process compared to x-ray-diffraction techniques and it has been successfully used in the past to determine the displacive or order-disorder character of ferroelectric transitions in related perovskites where ferroelectricity arises from CL [20]. In this paper we complement our previous structural characterization of the A -site ordered and disordered Ba-doped manganites (based on average synchrotron x-ray powder-diffraction measurements [10–12]) by means of a combined high-energy resolution fluorescence detected (HERFD) and total fluorescence yield (TFY) x-ray absorption spectroscopy (XAS) study to understand the alteration of the Mn local structure as a function of temperature, A -site cation size, and A -site randomness. The implication of these changes in the occurrence of charge-localized and polar states and the mechanism of the magnetoelectric transitions is determined.

II. EXPERIMENT SECTION

Polycrystalline ordered RBaMn_2O_6 ($R = \text{La}$, Nd , Sm , and Y) samples were prepared by solid-state chemistry method [10–12]. Stoichiometric amounts of dried La_2O_3 (or Nd_2O_3 , Sm_2O_3 , Y_2O_3), BaCO_3 , and Mn_2O_3 were mixed, ground, and heated at 1000 °C overnight. The resulting powder is reground, pressed into pellets, and sintered at 1250 °C in

TABLE I. Summary of crystal structures, magnetic ground state, and electric behavior for *A*-site disordered $R_{0.5}\text{Ba}_{0.5}\text{Mn}_2\text{O}_6$ and ordered $R\text{BaMn}_2\text{O}_6$ compounds. FM, AFM, M_{INH} , CG, and SG stand for ferromagnetic, antiferromagnetic, magnetically inhomogeneous, cluster glass, and spin glass, respectively. T_S is the temperature of the structural transitions. MIT denotes metal-insulator-like transition without charge segregation. CL indicates charge-localization transition associated with a charge segregation. Polar space groups are highlighted in bold.

<i>R</i> ion	La ³⁺	Pr ³⁺	Nd ³⁺	Sm ³⁺	Y ³⁺
$r_{R^{3+}}/r_{\text{Ba}^{2+}}$	0.845	0.82	0.79	0.77	0.68
A-site disordered $R_{0.5}\text{Ba}_{0.5}\text{Mn}_2\text{O}_6$					
Crystal structure	Cubic <i>Pm-3m</i>	Cubic <i>Pm-3m</i>	Cubic <i>Pm-3m</i>	Cubic <i>Pm-3m</i>	Cubic <i>Pm-3m</i>
Magnetic ground state	FM ($T_C = 279$ K)	M_{INH} FM+CG	M_{INH} FM+CG	SG ($T_{\text{SG}} = 45$ K)	SG ($T_{\text{SG}} = 45$ K)
A-site ordered $R\text{BaMn}_2\text{O}_6$					
Crystal structure	Tetragonal <i>P4/mmm</i>	Tetragonal <i>P4/mmm</i>	Tetragonal <i>P4/mmm</i>	Orthorhombic <i>Cmmm</i>	Monoclinic <i>C2/m</i>
		↓ Orthorhombic <i>P2₁am</i> ($T_S = 250$ K)	↓ Orthorhombic <i>Cmmm</i> ($T_S = 340$ K) ↓ Orthorhombic <i>P2₁am</i> ($T_S = 290$ K)	↓ Orthorhombic <i>Pnma</i> ($T_S = 380$ K) ↓ Orthorhombic <i>P2₁am</i>* ($T_S = 190$ K)	↓ Monoclinic <i>P2₁/c</i> ($T_S = 512$ K) ↓ Monoclinic <i>P2₁/n</i> ($T_S = 460$ K) ↓ Monoclinic <i>P2₁</i> ($T_S = 200$ K)
Magnetic ground state	FM ($T_C = 329$ K)	AFM ($T_N = 245$ K)	AFM ($T_N = 290$ K)	AFM ($T_N = 260$ K)	AFM ($T_N = 200$ K)
Electric behavior	Metallic	MIT ($T_{\text{MI}} = 245$ K)	MIT ($T_{\text{MI}} = 290$ K)	CL ($T_{\text{CL}} = 380$ K)	CL1 ($T_{\text{CL1}} = 512$ K) ↓ CL2 ($T_{\text{CL2}} = 460$ K) ↓ CL3 ($T_{\text{CL3}} = 200$ K)

*In the orthorhombic *P2₁am* polar phase of $\text{SmBaMn}_2\text{O}_6$, the orthorhombic *a*-axis is doubled compared to that in $\text{PrBaMn}_2\text{O}_6$ and $\text{NdBaMn}_2\text{O}_6$ compounds.

a gas flow of H_2/Ar mixture (2% H_2) saturated in water vapor to achieve a reductive atmosphere ($P_{\text{O}_2} \approx 10^{-11}$ bar). This is required to prevent the formation of the BaMnO_3 impurity [8]. Then, pellets are reground, pressed again into pellets, and sintered at 1375 °C for 24 h in the same atmosphere. After this step, the materials are oxygen deficient, $R\text{BaMn}_2\text{O}_{5+\delta}$ with $\delta \approx 0.1$. The next step consists of topotactic oxidation at 450 °C in an oxygen current flow for 24 h, which yields the stoichiometric $R\text{BaMn}_2\text{O}_6$ compounds.

Polycrystalline stoichiometric disordered $R_{0.5}\text{Ba}_{0.5}\text{MnO}_3$ samples were obtained by sintering pellets of the stoichiometric mixture of the corresponding oxides at 1400 °C in a flow of pure Ar for 24 h followed by a quenching in the same atmosphere. The resulting products were annealed for 16 h in an oxygen current flow followed by slow cooling (2 °C/min) down to room temperature. The annealing temperature was varied depending on the *R* type to avoid the formation of the BaMnO_3 impurity (850 °C and 800 °C for Y- and Sm-based

samples, respectively, and 750 °C for the other three compounds).

The polycrystalline samples were analyzed by powder x-ray diffraction, being single phase without detectable impurities. The chemical composition of the powders was also tested using wavelength-dispersive x-ray fluorescence spectrometry (Advant'XP+ model from Thermo-ARL), and the *R*:Ba:Mn stoichiometry agreed with the expected values within the experimental error (1%). The degree of *A*-site disorder was also checked by x-ray diffraction. Superstructure (0, 0, 1/2)_{cubic} reflections were only observed within the detection limit of our x-ray-diffraction measurements in the *A*-site ordered samples. In addition, all the disordered samples show the cubic *Pm-3m* structure expected for a random distribution of *R*/*Ba* atoms at the *A* site of $R_{0.5}\text{Ba}_{0.5}\text{MnO}_3$. As a representative example, the XRD patterns of YBaMn_2O_6 and $\text{Y}_{0.5}\text{Ba}_{0.5}\text{MnO}_3$ samples are compared in Fig. S2 in the Supplemental Material [21]. Perovskite structures of the *A*-

site ordered and disordered manganites shown in Fig. 1 are drawn by the program VESTA [22].

Magnetic measurements were carried out with a commercial Quantum Design (SQUID) magnetometer. The dc magnetization was measured between 5 and 400 K at an external magnetic field of 1 kOe for both ordered $R\text{BaMn}_2\text{O}_6$ and disordered $R_{0.5}\text{Ba}_{0.5}\text{MnO}_3$ series with $R = \text{La}, \text{Nd},$ and Sm . For the YBaMn_2O_6 and $\text{Y}_{0.5}\text{Ba}_{0.5}\text{MnO}_3$ samples, the dc magnetization was measured between 5 and 700 K at 1 kOe and field-cooled magnetization at 1 kOe was also recorded for the $\text{Y}_{0.5}\text{Ba}_{0.5}\text{MnO}_3$ compound. Calorimetric measurements were made in the ordered $R\text{BaMn}_2\text{O}_6$ ($R = \text{Sm}$ and Y) compounds using a Q2000 differential scanning calorimeter (DSC) from TA Instruments in the temperature range from 200 to 575 K. Powder samples (between 10–40 mg) sealed in aluminum hermetic pans were heated and cooled at a scanning rate of 10 K/min. Enthalpy and temperature calibrations were performed using standard indium and its melting transition. Differences on onset temperature and latent heat with respect to the expected values were lower than 0.1 K and 1%, respectively.

HERFD-XAS measurements at the Mn K edge were performed at the CLAES beamline [23] of the ALBA Synchrotron (Cerdanyola del Vallès, Spain) using a Si (311) double-crystal monochromator. HERFD-XAS spectra were collected in backscattering geometry at the maximum of the Mn $K\beta_{1,3}$ (6490 eV) emission line using the CLEAR spectrometer [24]. The overall energy resolution was determined to be 0.5 eV from the full width at half maximum of the quasielastic peak collected from a Kapton tape. A liquid- N_2 cryostat was used for the temperature-dependent measurements between 80 and 600 K. Standard transmission-detected EXAFS spectra were recorded in the La and Y compounds as the signal does not interfere with R L edges. For $R = \text{Nd}$ and Sm , EXAFS spectra were obtained by recording simultaneously the HERFD-XAS at the Mn $K\beta_{1,3}$ line and the TFY-XAS spectra measured with a Si diode. Following the procedure discussed by Lafuerza *et al.* [25,26], EXAFS spectra free of R self-absorption at the L edges can be obtained from the weighted addition of the HERFD- and TFY-XAS spectra, where the R self-absorption appears as negative and positive contributions [27], respectively. The fitted weight of each spectrum to suppress the R self-absorption was 75% (HERFD-XAS)+25% (TFY-XAS) for $R = \text{Nd}$ and 64% (HERFD-XAS)+36% (TFY-XAS) for $R = \text{Sm}$. This procedure is further discussed and illustrated in the Supplemental Material [21]. The HERFD-XAS spectra in the near-range energy range were normalized to the unity mean value in the high-energy (~ 6630 eV) part of the spectrum and all the EXAFS data were reduced using the standard procedures of the ATHENA software of the DEMETER package [28].

III. RESULTS AND DISCUSSION

A. Effects of the structural order/disorder on the magnetic properties

The magnetization curves as a function of temperature, $M(T)$, measured under 1 kOe for ordered and disordered samples are shown in Fig. 2. Strong differences are observed in compounds with the same nominal composition

depending on the degree of A -site ordering. It is clearly seen that a decrease in the degree of A -site order results in a decrease of the magnetic phase transitions temperature. Both disordered $\text{La}_{0.5}\text{Ba}_{0.5}\text{MnO}_3$ and ordered $\text{LaBaMn}_2\text{O}_6$ show a FM metallic ground state [Fig. 2(a)]. However, the transition temperature is $T_C = 329$ K in $\text{LaBaMn}_2\text{O}_6$ and about 50 K lower in disordered $\text{La}_{0.5}\text{Ba}_{0.5}\text{MnO}_3$, in agreement with previous reports [8,18]. On decreasing the ionic radius of the R atom, the competition between FM/metal and AFM/charge(orbital)-order behaviors arises and for ordered $\text{NdBaMn}_2\text{O}_6$, the $M(T)$ dependence reveals a sharp peak in accordance with previous studies [18,29]. The shape of the magnetization curve indicates that this competition is maximum in $\text{NdBaMn}_2\text{O}_6$, which shows the onset of a paramagnetic-to-FM transition at about 293 K, followed by a sudden AFM transition accompanied by the large reduction of $M(T)$ [Fig. 2(b)]. The neutron-diffraction study confirms the development of an A -type AFM order at $T_N = 290$ K [29]. Above this magnetic transition, FM correlations are still present although long-range FM ordering is not established. On the other hand, the disordered $\text{Nd}_{0.5}\text{Ba}_{0.5}\text{MnO}_3$ shows an increase of the magnetization below 250 K. The shape of the $M(T)$ curve illustrates a broad FM transition which suggests a certain degree of magnetic inhomogeneity in this sample. The decrease in magnetization at low temperature also indicates a glassy behavior. The most plausible scenario is the presence of FM clusters of different sizes (and/or different disorder degree) that are consecutively ordered as the temperature decreases. The presence of several FM transitions has also been observed for partially disordered Pr-based manganites [30]. This suggests that partial disorder favors a FM state for $R = \text{Pr}$ and Nd , coming from the lowering of the two-dimensional structural anisotropy caused by the layer-type order of R/Ba with the correspondent enhancement of isotropic double-exchange interactions [13,18]. On further decreasing the ionic radius of the R atom, the structural (CL) and magnetic transitions of the ordered compounds are decoupled. While the charge-localization transition temperature (T_{CL}) increases with decreasing R , the magnetic phase transitions temperatures continuously decrease and the ground state is AFM. For ordered $\text{SmBaMn}_2\text{O}_6$, the CE-type AFM transition occurs at $T_N = 260$ K like previously found in powder samples [31] [Fig. 2(c)]. However, an abrupt change in the $M(T)$ curve is observed at $T_{\text{CL}} \approx 385$ K. Finally, ordered YBaMn_2O_6 has the structural transition at $T_{\text{CL}} = 510$ K and shows a paramagnetic to an AFM transition at $T_N = 200$ K [18] [Fig. 2(d)]. Besides, below 45 K, a spin-glass-like behavior is reported that is correlated with the presence of a small amount of Y/Ba antisite occupancy [32]. On the other side, both disordered $\text{Sm}_{0.5}\text{Ba}_{0.5}\text{MnO}_3$ and $\text{Y}_{0.5}\text{Ba}_{0.5}\text{MnO}_3$ samples exhibit similar $M(T)$ curves [Figs. 2(c) and 2(d), respectively]: a paramagnetic behavior with a strong peak at low temperature in the zero-field-cooled measurement that disappears in field-cooled conditions, as shown for example for the Y-based compound in Fig. 2(d). This is typical of samples with disorder and competitive magnetic interactions. In this way, our results agree with previous reports on typical spin-glass behaviors in disordered $\text{Sm}_{0.5}\text{Ba}_{0.5}\text{MnO}_3$ and $\text{Y}_{0.5}\text{Ba}_{0.5}\text{MnO}_3$ samples [18,33]. Therefore, the decrease of the R ionic radius in the disordered manganites significantly

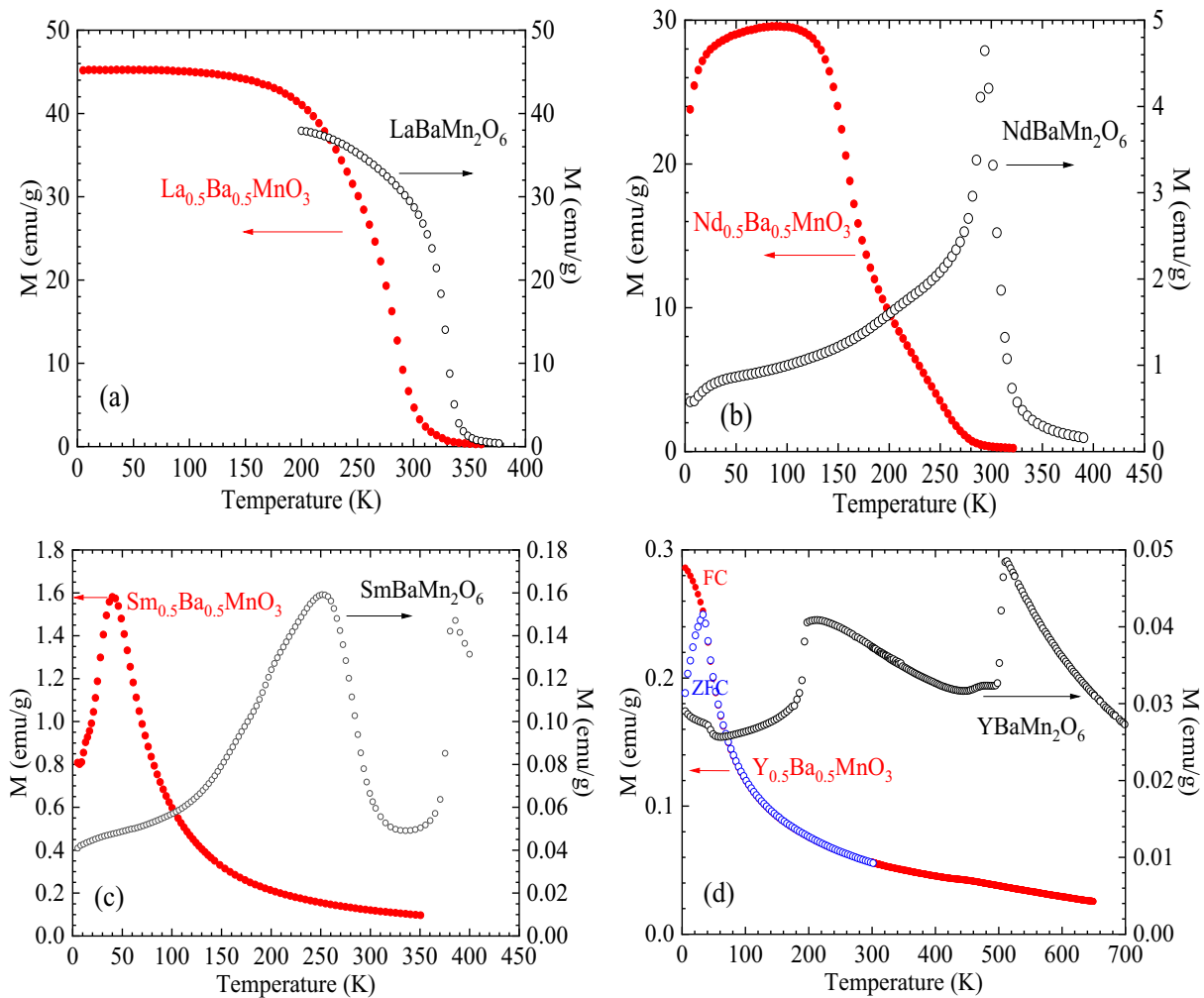


FIG. 2. Magnetization curves of polycrystalline ordered (open black circles) and disordered (closed red circles) $\text{LaBaMn}_2\text{O}_6$ (a), $\text{NdBaMn}_2\text{O}_6$ (b), $\text{SmBaMn}_2\text{O}_6$ (c), and YBaMn_2O_6 (d) samples as a function of temperature. Additionally, in (d) zero-field cooled (ZFC, open blue circles) together with field-cooled (FC, closed red circles) measurements are shown.

weakens the magnetic long-range order and no signs of CL transitions are observed [Table I and Fig. S1(b)]. However, in the ordered samples a long-range magnetic order is always realized whose nature changes from FM to A-type AFM and then CE-type AFM as the R size decreases. In addition, a structural (charge-localization) transition is strengthened with decreasing R size [Table I and Fig. S1(a)]. The different magnetic and polar phases observed in these manganites as a function of A -site order and average ionic radius clearly suggest an important effect of the Mn local structure distortions in understanding these phenomena.

B. Temperature dependence of the Mn local distortions

We now describe the behavior of the structural parameters derived from the Mn K -edge EXAFS analysis. The Fourier transforms (FTs) of the k^2 weighted EXAFS $\chi(k)$ signals in the k range between 2 and 12 \AA^{-1} as a function of temperature are shown for ordered $R\text{BaMn}_2\text{O}_6$ and disordered $R_{0.5}\text{Ba}_{0.5}\text{MnO}_3$ manganites in Figs. 3(a), 3(c), and 3(e) and Figs. 3(b), 3(d), and 3(f), respectively. The obtained FTs show many contributions up to $r = 6 \text{ \AA}$. The first intense

peak at about 1.5 \AA is associated with the Mn-O first shell. Further peaks around $2.6\text{--}4 \text{ \AA}$ are attributed to Mn- R /Ba and Mn-O-Mn paths that appear mixed up. At first look, evident differences in the local structure around the Mn atom are distinguished among the samples depending on the R type. Both ordered and disordered La-based samples show a monotonic increase of the peak's intensity when decreasing the temperature [Figs. 3(a) and 3(b)], corresponding to a progressive suppression of the thermal-induced dynamic disorder. For ordered $R\text{BaMn}_2\text{O}_6$ ($R = \text{Nd}$ and Sm), almost no temperature dependence of the FT peak's intensity is observed in contrast with their disordered counterparts [Figs. 3(c) and 3(d)], indicating the presence of a large static disorder that dominates the thermal-induced dynamic one. Finally, both ordered and disordered Y-based samples show the weakest peaks in agreement with their less-symmetrical crystallographic structure [Figs. 3(e) and 3(f)]. Although both Y samples show a slight decrease of the peak's intensity with increasing the temperature, the decrease is more gradual in the disordered compound.

The high-temperature crystallographic structures [10–12] of the different ordered $R\text{BaMn}_2\text{O}_6$ manganites (tetragonal

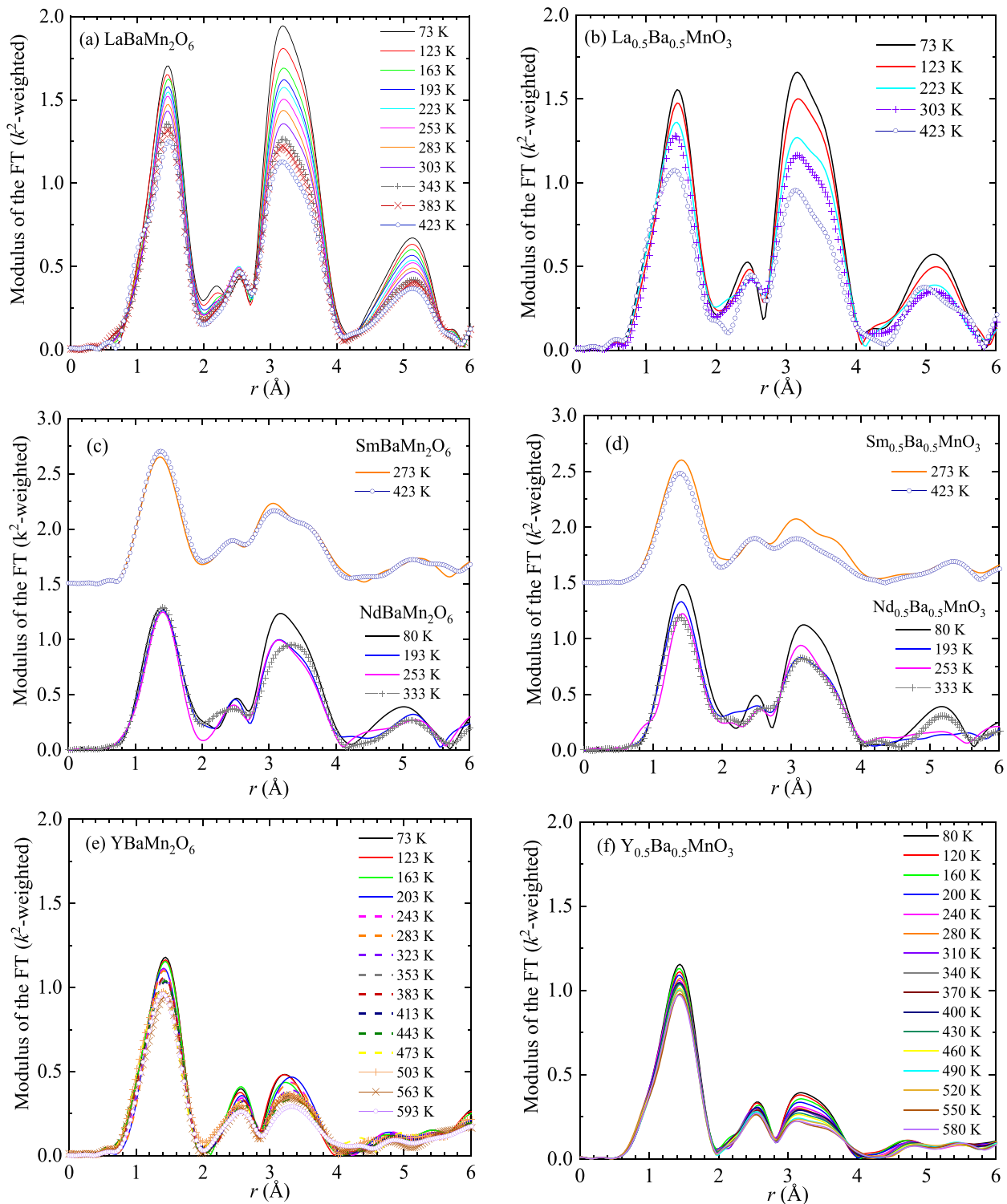


FIG. 3. Fourier transform of the k^2 -weighted $\chi(k)$ signals as a function of temperature for ordered $\text{LaBaMn}_2\text{O}_6$ (a); $\text{NdBaMn}_2\text{O}_6$ and $\text{SmBaMn}_2\text{O}_6$ (c); YBaMn_2O_6 (e) samples compared to the disordered $\text{La}_{0.5}\text{Ba}_{0.5}\text{MnO}_3$ (b); $\text{Nd}_{0.5}\text{Ba}_{0.5}\text{MnO}_3$ and $\text{Sm}_{0.5}\text{Ba}_{0.5}\text{MnO}_3$ (d); and $\text{Y}_{0.5}\text{Ba}_{0.5}\text{MnO}_3$ (f) ones.

$P4/mmm$ for $R = \text{La}$; monoclinic $Cmmm$ for $R = \text{Nd}$ and Sm , and monoclinic $C2/m$ for Y) were used as input to calculate and model the EXAFS signals. We found that Mn-O, Mn-R(Y), Mn-Ba, and Mn-Mn single-scattering paths contribute to the EXAFS spectrum, along with the three-leg Mn-O-Mn-Mn and four-leg Mn-O-Mn-O-Mn and the Mn-O-

O multiple-scattering paths. Fits of the k^2 -weighted EXAFS data were carried out in R space using theoretical functions from the FEFF6 code [34]. From the crystallographic structure viewpoint, the most significant difference between ordered $\text{R}\text{BaMn}_2\text{O}_6$ and disordered $\text{R}_{0.5}\text{Ba}_{0.5}\text{MnO}_3$ is the MnO_6 octahedron distortion, having a noncentrosymmetric deforma-

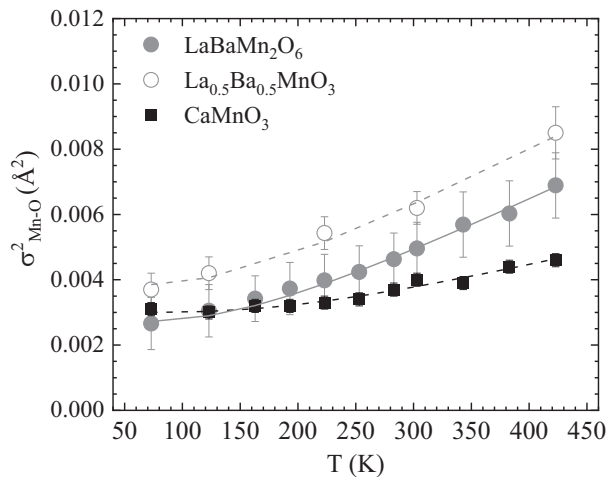


FIG. 4. Mn-O MSRD $\sigma^2(\text{\AA}^2)$ of ordered $\text{LaBaMn}_2\text{O}_6$ (full gray circles); disordered $\text{La}_{0.5}\text{Ba}_{0.5}\text{MnO}_3$ (empty gray circles), and the CaMnO_3 sample (full black squares), determined from a single-shell EXAFS analysis as a function of temperature. Lines represent the respective best-fit correlated Einstein models.

tion in the ground state for $R \neq \text{La}$ in the former compounds [Fig. 1(a)]. In this context, the EXAFS quantitative analysis was focused on the first coordination shell that is composed of 6 O atoms around the Mn absorber atom. The expected distortion at the polar and magnetic transitions is on the order of 0.1 \AA [10–12] that could not be resolved from our EXAFS data up to $k = 12 \text{ \AA}^{-1}$. Thus, different Mn-O distances possibly contributing to the first coordination shell are averaged and represented by one Mn-O distance with an averaged mean-square relative displacement (MSRD) factor (σ^2) and N the total coordination number fixed to 6 in the fits. An energy-origin shift (E_0) common for all the temperatures was also considered as fitting parameter and the many-body amplitude reduction factor S_0^2 was determined to be 0.75 from fitting the spectrum of the CaMnO_3 sample (regular MnO_6 octahedron) and fixed to this value for all the other samples. Moreover, the resulting average Mn-O interatomic distances are almost independent of temperature for all the samples.

In Fig. 4 we show the temperature evolution of best-fit σ^2 for the Mn-O first coordination shell in ordered $\text{LaBaMn}_2\text{O}_6$, disordered $\text{La}_{0.5}\text{Ba}_{0.5}\text{MnO}_3$, and CaMnO_3 compounds. In all three samples $\sigma_{\text{Mn-O}}^2$ has a nonstructured monotonic behavior with T . We did not find any anomaly at the ferromagnetic transition temperatures of the $\sigma_{\text{Mn-O}}^2$ factors, $T_C = 329 \text{ K}$ in $\text{LaBaMn}_2\text{O}_6$ and $T_C = 279 \text{ K}$ in disordered $\text{La}_{0.5}\text{Ba}_{0.5}\text{MnO}_3$. We have modeled the temperature dependence of these $\sigma_{\text{Mn-O}}^2$ considering two square-summed terms [35]: $\sigma^2(T) = \sigma_0^2 + \frac{\hbar^2}{2\mu k_B \theta_E} \coth\left(\frac{\theta_E}{2T}\right)$.

The static term (σ_0^2) is independent of temperature and proportional to the disorder around the absorbing atom. The dynamic term is related to the thermal vibrations; thus, its amplitude is temperature dependent and decreases as temperature does. To fit the dynamic term we use the correlated Einstein model, where μ is the reduced mass for the Mn-O bond pair and θ_E is the Einstein temperature. The $\sigma_{\text{Mn-O}}^2$ parameters for CaMnO_3 , with regular MnO_6 octahedra, are the lowest for all the temperatures and consistent with a standard thermal

temperature dependence (lattice vibrations). They are well described by a correlated Einstein model with an Einstein temperature $\theta_E = 650 \pm 30 \text{ K}$ and negligible static contribution from local distortion (Fig. 4, dashed black line). The temperature dependence of the $\sigma_{\text{Mn-O}}^2$ parameters for the A-site disordered cubic $\text{La}_{0.5}\text{Ba}_{0.5}\text{MnO}_3$ sample also agrees with a correlated Einstein model with negligible static contribution, but a smaller θ_E of about $450 \pm 20 \text{ K}$ is deduced (Fig. 4, dashed gray line). The decrease in θ_E indicates a softer Mn-O bond with respect to CaMnO_3 in agreement with the elongation of the average Mn-O distance from 1.88 to 1.93 \AA by replacing Ca by (La, Ba). Finally, the temperature evolution of $\sigma_{\text{Mn-O}}^2$ for the ordered $\text{LaBaMn}_2\text{O}_6$ sample was also fitted using the correlated Einstein model yielding a similar $\theta_E = 465 \pm 20 \text{ K}$ as for the disordered sample but a slightly negative value for the static term [$\sigma_0^2 = -0.0015(5)$] was found (Fig. 4, solid gray line). This negative value for the static term can be explained by considering that in the σ^2 results of the EXAFS fitting procedure there might be systematic errors giving rise to a displacement of the scale reference. Thus, this value cannot be used in an absolute way but only in the comparison to the disordered sample. This result indicates that the amount of static disorder in $\text{LaBaMn}_2\text{O}_6$ is slightly smaller than that displayed in its counterpart, $\text{La}_{0.5}\text{Ba}_{0.5}\text{MnO}_3$. In any case, both ordered and disordered La-based samples show an almost symmetric octahedron in the whole temperature range. We recall that both samples are long-range FM and metallic below T_C (Table I), which prevents the presence of localized lattice distortions at the Mn site in analogy with colossal magnetoresistive $\text{La}_{1-x}\text{Ca}_x\text{MnO}_3$ manganites [36]. However, the A-site disordered sample shows a reduced T_C consistent with the higher static disorder and the presence of a small amount of lattice polarons in the FM state, as revealed by neutron-scattering experiments [37].

In Fig. 5 we show the MSRD factor σ^2 for the Mn-O first coordination shell as a function of temperature for ordered RBaMn_2O_6 [$R = \text{Nd}$ and Sm ; Fig. 5(a)] and disordered $\text{R}_{0.5}\text{Ba}_{0.5}\text{MnO}_3$ [$R = \text{Nd}$ and Sm ; Fig. 5(b)] compounds compared to the best-fit Einstein models obtained above for their ordered and disordered La-based counterparts (gray lines), respectively. A quite similar temperature evolution of $\sigma_{\text{Mn-O}}^2$ is observed between $\text{NdBaMn}_2\text{O}_6$ ($T_{\text{MI}} = 290 \text{ K}$; full black squares) and $\text{SmBaMn}_2\text{O}_6$ ($T_{\text{CL}} = 380 \text{ K}$; full red triangles) samples even if only two temperature points could be measured in the latter [Fig. 5(a)]. We note here that in $\text{NdBaMn}_2\text{O}_6$, CL takes place coupled to the metal-insulator-like (MIT) transition at T_{MI} concomitant with structural and antiferromagnetic transitions (Table I) [10]. However, there is only one inequivalent site for the Mn atom in the low-temperature charge-localized polar phase (space group $P2_1am$) so charge segregation cannot account for the CL. Due to this fact, in Table I and Fig. 5(a), we have not denoted by T_{CL} but by T_{MI} the transition temperature for the Nd-ordered sample. At high temperatures above the CL transitions, the $\sigma_{\text{Mn-O}}^2$ for ordered $\text{NdBaMn}_2\text{O}_6$ and $\text{SmBaMn}_2\text{O}_6$ are fully consistent with the correlated Einstein model deduced for the La-ordered sample (solid gray line). No static contribution from disorder with respect to their high-temperature nonpolar phases was found in this temperature range. However, differently from $\text{LaBaMn}_2\text{O}_6$, $\sigma_{\text{Mn-O}}^2$ increases for the ordered $\text{NdBaMn}_2\text{O}_6$ (or $\text{SmBaMn}_2\text{O}_6$) compound on cooling below

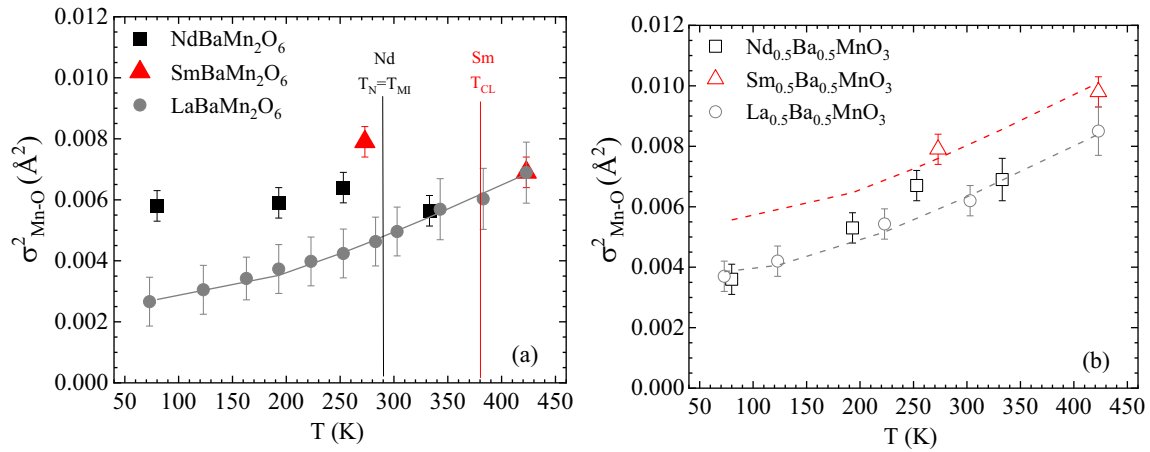


FIG. 5. (a) Mn-O MSRD $\sigma^2(\text{\AA}^2)$ of ordered LaBaMn₂O₆ (full gray circles), NdBaMn₂O₆ (full black squares), and SmBaMn₂O₆ (full red triangles) samples determined from a single-shell EXAFS analysis as a function of temperature. Gray solid line represent the best-fit correlated Einstein model for LaBaMn₂O₆. Charge localization (CL) in NdBaMn₂O₆ takes place at T_{MI} without charge segregation. (b) Mn-O MSRD $\sigma^2(\text{\AA}^2)$ of disordered La_{0.5}Ba_{0.5}MnO₃ (empty gray circles), Nd_{0.5}Ba_{0.5}MnO₃ (empty black squares), and Sm_{0.5}Ba_{0.5}MnO₃ (empty red triangles) samples determined from a single-shell EXAFS analysis as a function of temperature. Gray dashed line represents the best-fit correlated Einstein model for La_{0.5}Ba_{0.5}MnO₃, whereas red dashed line is this best-fit correlated Einstein model where a positive static disorder contribution has been added.

T_{MI} (or T_{CL}) and it remains almost constant with temperature down to 80 K in the case of Nd-based sample. This behavior can be associated with the CL. If there is a local distortion of the MnO₆ octahedron associated with the CL, then there must be an additional broadening contribution σ_{CL}^2 for the $\sigma_{\text{Mn-O}}^2$ that is zero above T_{CL} and increases as T is lowered below T_{CL} . We can then extract this σ_{CL}^2 contribution by subtracting from the experimental $\sigma_{\text{Mn-O}}^2$ data the phonon contribution calculated by the correlated Einstein model that fits the high-temperature data. Such σ_{CL}^2 contribution for ordered $R\text{BaMn}_2\text{O}_6$ ($R = \text{Nd}$ and Sm) is shown in Fig. 6. It is clear that the additional distortion in NdBaMn₂O₆ (full black squares) appears below the MIT (charge-localization) transition and remains almost constant on cooling down to 80 K. It also agrees with the occurrence of a first-order structural transition from the high-temperature nonpolar $Cmmm$

phase to a low-temperature polar $P2_1am$ phase coupled to the AFM transition at $T_N = 290$ K (Table I) [10]. Moreover, in SmBaMn₂O₆ a bigger σ_{CL}^2 distortion is anticipated at around 273 K (Fig. 6, full red triangles), i.e., in the charge-localized phase, which is consistent with the presence of significant charge segregation between the two distorted nonequivalent Mn sites in the $Pnma$ structure in contrast with the single distorted Mn site found in NdBaMn₂O₆.

For what concerns the disordered compounds [Fig. 5(b)], the $\sigma_{\text{Mn-O}}^2$ for Nd_{0.5}Ba_{0.5}MnO₃ (open black squares) roughly follows the correlated Einstein model obtained for the disordered La compound (dashed gray line). However, the magnetic properties of the Nd_{0.5}Ba_{0.5}MnO₃ sample [Fig. 2(b)] indicates that it is a partially disordered manganite so below 280 K there is a competition between regions with CL with an associated σ_{CL}^2 distortion contribution and FM regions where the local distortion gets quenched. We have estimated this additional σ_{CL}^2 distortion (open squares in Fig. 6), which follows a similar trend to that driven by the CL in the ordered sample (closed squares in Fig. 6) but below 250 K, it is found to be negligible again, in agreement with the development of FM contributions at $T_C = 170$ K. On the other hand, disordered Sm_{0.5}Ba_{0.5}MnO₃ displays a temperature evolution of $\sigma_{\text{Mn-O}}^2$ [open red triangles in Fig. 5(b)] that is well described by the correlated Einstein model as found in La_{0.5}Ba_{0.5}MnO₃ but adding a static disorder contribution of about $\sigma_0^2 = 0.0012(5) \text{\AA}^2$ [Fig. 5(b), dashed red line]. Besides that, no signature of additional σ_{CL}^2 distortion is found in Sm_{0.5}Ba_{0.5}MnO₃ (Fig. 6). We thus propose that the presence of a significant static disorder contribution in Sm_{0.5}Ba_{0.5}MnO₃ prevents the development of ferromagnetism in this sample in the whole temperature range (Table I).

Finally, we analyze the results for the other extreme of the series in terms of the R ionic radius, i.e., the Y-based samples. Figure 7 shows the temperature evolution of $\sigma_{\text{Mn-O}}^2$ for both ordered YBaMn₂O₆ and disordered Y_{0.5}Ba_{0.5}MnO₃ compounds, where a very similar dependence is obtained.

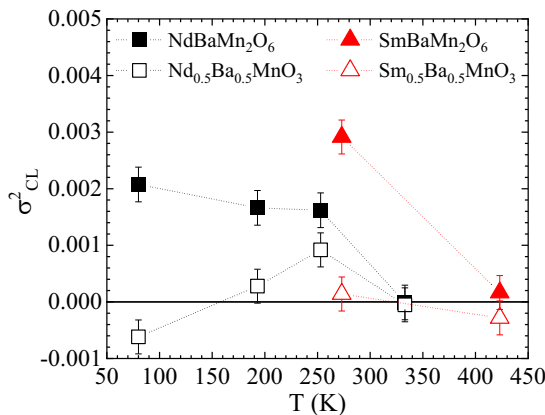


FIG. 6. Plot of $\sigma_{\text{CL}}^2(T)$ for the Mn-O bond length in ordered NdBaMn₂O₆ (full black squares) and SmBaMn₂O₆ (full red triangles) samples compared to the disordered Nd_{0.5}Ba_{0.5}MnO₃ (empty black squares) and Sm_{0.5}Ba_{0.5}MnO₃ (empty red triangles) ones. Dotted lines are a guide for the eye.

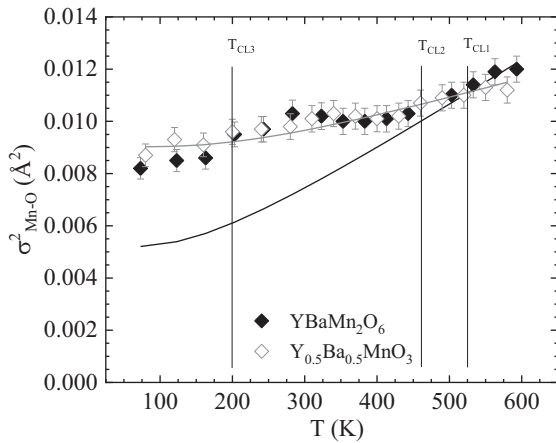


FIG. 7. Mn-O MSD $\sigma^2(\text{\AA}^2)$ of ordered YBaMn_2O_6 (full black diamonds) and disordered $\text{Y}_{0.5}\text{Ba}_{0.5}\text{MnO}_3$ (empty gray diamonds) samples determined from a single-shell EXAFS analysis as a function of temperature. Lines represent the respective best-fit correlated Einstein models as described in the text.

It is also well apparent that the $\sigma_{\text{Mn-O}}^2(T)$ parameters in these cases have a less steep dependence with T than the La-based samples (Fig. 4). Again, we have fitted the temperature evolutions of $\sigma_{\text{Mn-O}}^2$ with correlated Einstein models. For ordered YBaMn_2O_6 , a static $\sigma_0^2 = 0.0010(5) \text{\AA}^2$ contribution is found to be added to the correlated Einstein model with $\theta_E = 465 \pm 20 \text{ K}$ found for the La-based ordered sample at high temperatures above 450 K (black solid line in Fig. 7). This points to the presence of a local distortion of the MnO_6 octahedron already in the high-temperature phase above the CL transitions. We have then evaluated the temperature dependence of the σ_{CL}^2 component by subtracting the phonon contribution calculated with the correlated Einstein model from the experimental data, which is shown in Fig. 8. σ_{CL}^2 remains almost constant with temperature on cooling down to 450 K and below this temperature slightly increases, reaching the maximum value in the temperature range below 300 K. This increment agrees with the occurrence of the structural (CL) transition observed at 460 K by synchrotron x-ray

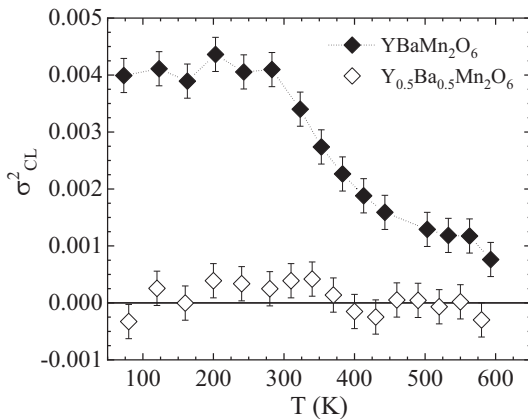


FIG. 8. Plot of $\sigma_{\text{CL}}^2(T)$ for the Mn-O bond length in ordered YBaMn_2O_6 (full black diamonds) compared to the disordered $\text{Y}_{0.5}\text{Ba}_{0.5}\text{MnO}_3$ (empty black diamonds) Dotted lines are a guide for the eye.

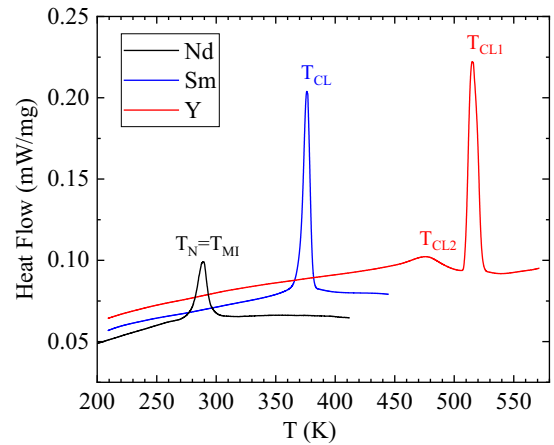


FIG. 9. Differential scanning calorimetry of $\text{NdBaMn}_2\text{O}_6$, $\text{SmBaMn}_2\text{O}_6$, and YBaMn_2O_6 measured by heating at 20 K/min in the temperature regions surrounding the polar CL transitions (Sm, Y) and the antiferromagnetic metal-insulator transition (Nd).

diffraction (Table I) [12], giving rise to four nonequivalent Mn sites that can be grouped in two pairs in terms of charge segregation and thus preserving the checkerboard arrangement in the ab plane. Below $T_N \sim 200 \text{ K}$, another structural transition is observed coupled to the AFM transition in the ordered sample into a polar $P2_1$ phase [12], which is not reflected in σ_{CL}^2 . For the disordered $\text{Y}_{0.5}\text{Ba}_{0.5}\text{MnO}_3$ compound, however, we do not see any changes in the magnetization with temperature that suggest the formation of a charge-localized state in this sample in the whole temperature range (Fig. 2). Thus, the nearly temperature-independent behavior of $\sigma_{\text{Mn-O}}^2$ in $\text{Y}_{0.5}\text{Ba}_{0.5}\text{MnO}_3$ can be well described by a correlated Einstein model but with a rather high $\theta_E = 690 \pm 50 \text{ K}$ (similar to the Einstein temperature of CaMnO_3) plus a huge static disorder $\sigma_0^2 = 0.0062(5) \text{\AA}^2$ (gray solid line in Fig. 7). Therefore, the much weaker temperature dependence of $\sigma_{\text{Mn-O}}^2$ in this sample is related to the presence of this huge static disorder and may explain the fact that no magnetic order develops (Table I).

The present EXAFS results suggest both, order-disorder and displacive mechanisms, contribute to the CL and polar structural transitions in ordered $R\text{BaMn}_2\text{O}_6$ compounds depending on the R atom. To gain insights on the particular mechanism as a function of the A -site cation, the entropy variation (ΔS) connected with the high-temperature structural transformations has been determined for $\text{SmBaMn}_2\text{O}_6$, YBaMn_2O_6 , and $\text{NdBaMn}_2\text{O}_6$. The DSC curves of these ordered perovskites measured on heating from 200 K are shown in Fig. 9. In $\text{SmBaMn}_2\text{O}_6$ only an endothermic peak at $T_{\text{CL, Sm}} = 380 \text{ K}$ has been detected (Fig. 9, blue line), corresponding to the structural transition from the low-temperature phase ($Pnam$) to the high-temperature phase ($Cmmm$) coupled with the first CL transition (Table I) [11]. The calculated entropy content, $\Delta S_{\text{exp, Sm}}$, is $7.8 \pm 0.2 \text{ J/mol K}$. In YBaMn_2O_6 two successive endothermic peaks were observed at $T_{\text{CL2, Y}} = 475 \text{ K}$ and $T_{\text{CL1, Y}} = 515 \text{ K}$ (Fig. 9, red line). For this sample, the total calculated entropy variation is $\Delta S_{\text{exp, Y}} = \Delta S_{\text{exp, Y}}(T_{\text{CL1, Y}}) + \Delta S_{\text{exp, Y}}(T_{\text{CL2, Y}}) = 7.3 \pm 0.2 \text{ J/mol K}$. The narrow and large heat-capacity peak

at T_{CL1} is associated with the structural transition between the two monoclinic structures at ~ 500 K in YBaMn_2O_6 , that is, from a $P2_1/c$ cell to the $C2/m$ cell [12]. The entropy content for this phase transition $\Delta S_{\text{exp}, Y}(T_{CL1, Y})$ is about 5.94 ± 0.15 J/mol K while for the second transition at T_{CL2} is about 1.36 ± 0.2 J/mol K. This latter anomaly corresponds to the structural transition between the $P2_1/n$ and $P2_1/c$ structures, coupled with the second CL transition. It is seen that the experimental values of total entropy variation for both compounds are similar within the experimental error, mainly related with the selection of the subtracted baseline, $0.93R$ for $\text{SmBaMn}_2\text{O}_6$ and $0.88R$ for YBaMn_2O_6 . On the other hand, in $\text{NdBaMn}_2\text{O}_6$ the calculated entropy content associated with the endothermic peak observed at $T_N = T_{MI} = 290$ K (Fig. 9, black line) is $\Delta S_{\text{exp}, Nd} = 4.5 \pm 0.1$ J/mol K, which is the lowest of the three ordered samples.

When analyzing the entropy change, the coupling between spin, charge, and orbital states in the structural transition gives rise to several contributions to the total entropy content [38], which complicates the interpretation of the experimental entropy content at the transition. This is the case of $\text{NdBaMn}_2\text{O}_6$, where there are three expected overlapped contributions: local distortions, electronic localization, and magnetic order. Nonetheless, the entropy change in $\text{NdBaMn}_2\text{O}_6$ corresponds to only $\Delta S = 0.55R$, which is the smallest of the three samples. There are several effects that can contribute to a reduction in the entropy content of this transition, such as strong magnetic correlations above T_N or the mass enhancement of carriers above T_{MI} . In any case, the relatively small ΔS value seems to be related to the lack of charge segregation in the Mn sublattice for $\text{NdBaMn}_2\text{O}_6$ and the exact quantification of the different contributions is beyond the scope of the present work. Therefore, we focus on $\text{SmBaMn}_2\text{O}_6$ and YBaMn_2O_6 compounds, where contributions coming from magnetic and orbital ordering are not present in the high-temperature structural (CL) transformations. If only CL between two nonequivalent Mn sites is involved, the expected entropy variation would be $\Delta S_{CL} = 2R \ln 2 = 1.39R = 11.53$ J/mol K. Thus, for the Sm and Y compound, the experimental ΔS values are only 32 and 37% smaller than ΔS_{CL} , respectively. If any other contribution was negligible, the presence of short-range order CL above T_{CL} could account for the remaining entropy on $\text{SmBaMn}_2\text{O}_6$ and YBaMn_2O_6 . However, no evidence of this short-range order charge localization can be inferred from our EXAFS and DSC measurements. A more detailed study by adiabatic calorimetry could help to discard this possibility.

Another possible origin for the discrepancy between experimental and theoretical entropies has been discussed by Sedmidubský *et al.* [39], in their work on the $\text{Bi}_{1-x}\text{Sr}_x\text{MnO}_3$. The above theoretical entropy content is based on considering a perfect charge segregation ($\Delta q = 1e^-$) and that Mn^{3+} and Mn^{4+} ions are present and ordered. They discuss that the theoretical entropy variation could be larger than the experimental value if the charge segregation is smaller than the perfect ionic case and then a mixed-valence behavior is still present in the charge-ordered phase. This has also been considered as a possible explanation for the entropy discrepancy in YBaFe_2O_5 at the Verwey transition [40], where the experimental entropy is 26% lower than the theoretical expected value. This clearly

happens in our YBaMn_2O_6 compound since a small charge segregation of around $\Delta q = 0.05\text{--}0.12e^-$ at $T_{CL1, Y}$ which reaches a maximum value of $\Delta q = 0.4e^-$ below $T_{CL2, Y}$ is determined [12]. However, for $\text{SmBaMn}_2\text{O}_6$ compound, charge localization at $T_{CL, Sm}$ is close to a perfect ionic description but it decreases rapidly down to $\Delta q = 0.33e^-$ as the temperature decreases [11].

Finally, the most plausible explanation is an order-disorder mechanism. If an order-disorder of a local distortion is assumed to drive these structural (CL) transitions, the theoretical entropy variation would be $\Delta S = R \ln 2 = 0.695R = 5.76$ J/mol K, very close to the experimental entropy variation found for the first structural transition from $C2/m \rightarrow P2_1/c$ structures at around $T_{CL1, Y} = 515$ K in YBaMn_2O_6 . This order-disorder mechanism can be then understood as follows: Above $T_{CL1, Y}$, there is only one Mn site that is already distorted with two local disorder positions for the oxygen atoms of the MnO_6 that are randomly occupied in the disordered model (or dynamically disordered). On cooling, the transition involves cooperative tilts of the MnO_6 octahedra that order the oxygen atomic shifts in opposite directions for the two nonequivalent Mn sites but without any significant charge segregation, i.e., no change in the MnO_6 distortion. Moreover, the remaining small entropy content ($0.16R$) of the second structural transition at $T_{CL2, Y} = 476$ K is likely to correspond to a displacive phenomenon involving a breathing oxygen-distortion mode that leads to two differently distorted Mn sites, in agreement with a charge segregation of $0.4e^-$. In $\text{SmBaMn}_2\text{O}_6$, both order-disorder of local distortions and displacive mechanisms should be simultaneously involved at the structural transition at $T_{CL, Sm} = 380$ K in order to account for the total entropy variation. This is supported by the structural x-ray study [11] since the phase transition is mediated by cooperative tilts of the MnO_6 octahedra together with a series of breathing- and asymmetric-stretching oxygen-distortion modes.

C. Effects of the structural order/disorder on the Mn electronic structure

To provide further characterization of the nature of the fractional-mixed valence state of Mn in these manganites, we have analyzed the x-ray absorption near-edge structure (XANES) spectral signatures of both ordered $\text{R}\text{BaMn}_2\text{O}_6$ and disordered $\text{R}_{0.5}\text{Ba}_{0.5}\text{Mn}_2\text{O}_6$ samples as a function of the R cation. The Mn $K\beta$ -detected HERFD-XANES spectra for ordered $\text{R}\text{BaMn}_2\text{O}_6$ and disordered $\text{R}_{0.5}\text{Ba}_{0.5}\text{Mn}_2\text{O}_6$ compounds with $R = \text{Nd}, \text{Sm},$ and Y at 80 K are presented in Fig. 10(a) and Fig. 10(b), respectively. Differently, transmission-detected XANES spectra were recorded for ordered/disordered samples with $R = \text{La}$ and Y . Although the HERFD-XANES technique provides high-energy resolution beyond that achievable with conventional core-hole lifetime broadened transmission-detected XANES measurements [41], at the Mn K edge the line sharpening is moderate and we can reliably compare XANES spectra obtained by the two different detection modes, as shown in the Supplemental Material [21] (Fig. S5).

Although all XANES spectra, for both ordered and disordered samples, lie intermediate between those of NdMnO_3

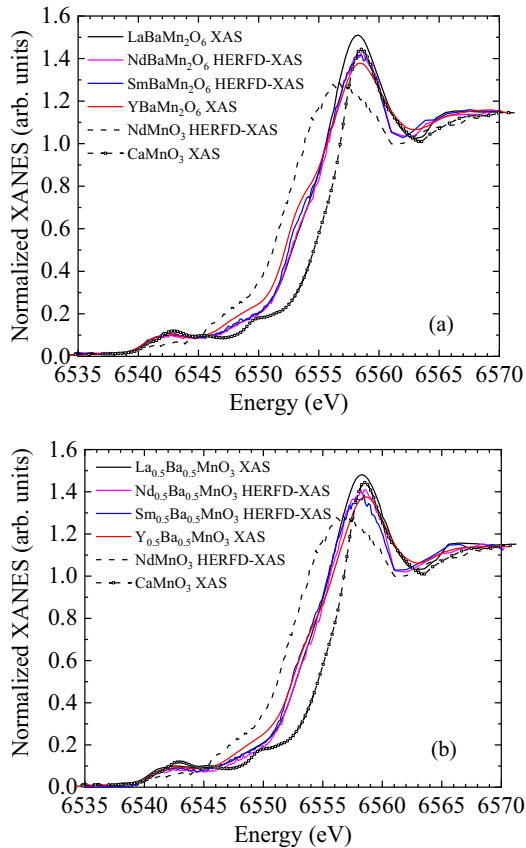


FIG. 10. (a) Mn $K\beta$ -detected HERFD-XANES spectra of ordered $R\text{BaMn}_2\text{O}_6$ ($R = \text{Nd}$ and Sm) samples in comparison with standard transmission XANES spectra of $\text{LaBaMn}_2\text{O}_6$ and YBaMn_2O_6 at $T = 80$ K ($T = 273$ K for Sm -based sample). (b) Mn $K\beta$ -detected HERFD-XANES spectra of disordered $R_{0.5}\text{Ba}_{0.5}\text{MnO}_3$ ($R = \text{Nd}$ and Sm) samples in comparison with standard transmission XANES spectra of $\text{La}_{0.5}\text{Ba}_{0.5}\text{MnO}_3$ and $\text{Nd}_{0.5}\text{Ba}_{0.5}\text{MnO}_3$ at $T = 80$ K ($T = 273$ K for Sm -based sample). Mn $K\beta$ -detected HERFD-XANES spectrum of NdMnO_3 and transmission XANES spectrum of CaMnO_3 as references for the formally Mn^{3+} and Mn^{4+} , respectively, are also reported for comparison.

(Mn^{3+}) and CaMnO_3 (Mn^{4+}) references, as expected for 50% R doping at the Ba site, a closer look into the spectral line shape reveals important differences. Figure 10(a) clearly shows that YBaMn_2O_6 and $\text{SmBaMn}_2\text{O}_6$ ordered samples feature a step in the center of the edge at 80 K, signature of the presence of two distinct Mn sites as expected for a charge-ordered (-localized) state. This step is not so clear for $\text{NdBaMn}_2\text{O}_6$ and $\text{LaBaMn}_2\text{O}_6$ ordered samples, both showing a more uniform slope of the main edge. In $\text{LaBaMn}_2\text{O}_6$, this is consistent with its metallic ferromagnetic state while for $\text{NdBaMn}_2\text{O}_6$, the lack of sensitivity in the XANES spectrum is perfectly understood in terms of the single site for the Mn atom in its $P2_1am$ cell [10], which also agrees with the tiny local distortion of the MnO_6 octahedron found by EXAFS. Finally, the slope of the main edge is sharper for the disordered samples [Fig. 10(b)] compared with the ordered ones in agreement with the lack of charge-localized states.

IV. CONCLUSIONS

The relationship between the Mn local structure and the charge-localized and polar phases of A -site ordered/disordered $R\text{BaMn}_2\text{O}_6/R_{0.5}\text{Ba}_{0.5}\text{Mn}_2\text{O}_6$ ($R = \text{La}$, Nd , Sm , and Y) has been investigated to provide further insights on the mechanisms driving these phases. For the largest average ionic size of the A site, $R = \text{La}$, both ordered/disordered manganites show a FM metallic behavior without any charge-localized or polar phases. In this case, the increase of A -site disorder only weakens the FM behavior. EXAFS measurements indicate the presence of regular MnO_6 octahedra in agreement with the development of long-range ferromagnetism coupled to the metallic behavior in both ordered and disordered La -based manganites, similarly to the colossal magnetoresistance manganites [42]. Following a decreasing in the average ionic size of the A site, in $\text{NdBaMn}_2\text{O}_6$ the steep onset of the FM state around 300 K is followed by an A -type AFM transition at $T_N = 290$ K coupled to a metal to insulator-like (electronic localization) transition. EXAFS results confirm the occurrence of a tiny local distortion of the MnO_6 octahedra below T_N , characteristic of a charge-localized phase, but without a significant charge segregation in agreement with the occurrence of a single site for the Mn atom in the low-temperature polar structure. In contrast, A -site disorder in $\text{Nd}_{0.5}\text{Ba}_{0.5}\text{MnO}_3$ not only tends to weaken the long-range FM order but also enhances the competition between ferromagnetism and CL promoting a glassy behavior. Such a competition is clearly reflected in the local structure around the Mn site. A smaller local distortion of the MnO_6 than in the ordered counterpart appears at 253 K, which is completely suppressed on cooling below 200 K, thus favoring the FM contributions at low temperatures. A bigger local distortion than in $\text{NdBaMn}_2\text{O}_6$ is found by EXAFS in $\text{SmBaMn}_2\text{O}_6$ at 273 K (below $T_{CL} \approx 380$ K). However, the MnO_6 local structure of the A -site disordered $\text{Sm}_{0.5}\text{Ba}_{0.5}\text{MnO}_3$ shows an additional temperature-independent disorder contribution in the temperature range between 473 and 273 K, which can be at the origin of the absence of long-range magnetic order. Since the local distortion of the MnO_6 octahedron in Nd - and Sm -ordered samples develops below their CL and polar transitions, the EXAFS results point to a displacive mechanism driving these transitions. Finally, for the smallest A -site cation, in YBaMn_2O_6 the biggest local distortion of the MnO_6 octahedron is found by EXAFS, already in the high-temperature phase above the first structural (CL) transition ($T_{CL1} \approx 500$ K). This local distortion remains almost constant with decreasing the temperature across T_{CL1} down to about 450 K. Therefore, an order-disorder mechanism driving this first structural (CL) transition is suggested. Below this temperature, it slightly increases again and remains almost constant down to the lowest temperature, even below the polar transition at $T_{CL3} \sim 200$ K in agreement with the presence of AFM correlations. These results would be consistent with an additional small displacive contribution to the second CL transition at $T_{CL2} \approx 460$ K. Moreover, the disordered $\text{Y}_{0.5}\text{Ba}_{0.5}\text{MnO}_3$ also shows the largest static disorder contribution in the high-temperature phase that remains constant upon cooling in the whole temperature range, which is in agreement with the absence of any magnetic order also in this

disordered sample. Besides, entropy contents in connection with the previous EXAFS results allow us to conclude that the CL and/or polar character of the structural transitions in ordered RBaMn_2O_6 ($R = \text{Sm}$ and Y) samples results from a combination of order-disorder and displacive phenomena.

In conclusion, for the A -site ordered RBaMn_2O_6 samples with R cations smaller than La , both, A -site order and a sufficiently large difference in the ionic size between Ba and R cations at the A site favor the development of local distortions of the MnO_6 octahedra at higher temperatures, even above the structural CL transitions. These local distortions result in the occurrence of charge segregation that is detrimental for the development of long-range FM order but allows for the presence of polar phases.

ACKNOWLEDGMENTS

The authors would like to acknowledge the use of Servicio General de Apoyo a la Investigación from Universidad de Zaragoza and Servicio de Calorimetría y Análisis Térmico of the INMA institute. Granted beam time at BL22 (CLAESS) beam line at ALBA synchrotron is acknowledged (Project No. 2018022760). For financial support, we thank the Spanish Ministerio de Ciencia, Innovación y Universidades (Projects No. RTI2018-098537-B-C22 and No. PID2021-124734OB-C21 cofunded by ERDF from EU). G.G. acknowledges Grant No. FJC2020-044866-I funded by Project MCIN/AEI/10.13039/501100011033 and by the “European Union Next Generation EU/PRTR”.

- [1] S. Jin, T. H. Tiefel, M. McCormack, R. A. Fastnacht, R. Ramesh, and L. H. Chen, Thousandfold change in resistivity in magnetoresistive La-Ca-Mn-O films, *Science* **264**, 413 (1994).
- [2] *Colossal Magnetoresistance, Charge Ordering and Related Properties of Manganese Oxides*, edited by C. N. R. Rao and B. Raveau (World Scientific, Singapore, 1998).
- [3] Y. Tokura, Critical features of colossal magnetoresistive manganites, *Rep. Prog. Phys.* **69**, 797 (2006).
- [4] J. C. Debnath, R. Zeng, J. H. Kim, and S. X. Dou, Giant magnetic entropy change in colossal magnetoresistance in $\text{La}_{0.7}\text{Ca}_{0.3}\text{MnO}_3$ material in low field, *J. Appl. Phys.* **107**, 09A916 (2010).
- [5] L. K. Joy, S. S. Samatham, S. Thomas, V. Ganesan, S. Al-Harhi, A. Liebig, M. Albrecht, and M. R. Anantharaman, Colossal thermoelectric power in charge ordered lanthanum calcium manganites ($\text{La}_{0.5}\text{Ca}_{0.5}\text{MnO}_3$), *J. Appl. Phys.* **116**, 213701 (2014).
- [6] D. V. Efremov, J. van den Brink, and D. I. Khomskii, Bond-versus site-centred ordering and possible ferroelectricity in manganites, *Nat. Mater.* **3**, 853 (2004).
- [7] Y. Taguchi *et al.*, Emergent phenomena in perovskite-type manganites, *Physica B* **407**, 1685 (2012).
- [8] F. Millange, V. Caignaert, B. Domenges, and B. Raveau, Order-disorder phenomena in new $\text{LaBaMn}_2\text{O}_{6-x}$ CMR perovskites, crystal and magnetic structure, *Chem. Mater.* **10**, 1974 (1998).
- [9] V. S. Trukhanov, O. I. Toyanchuk, M. Hervieu, H. Szymczak, and K. Barner, Magnetic and electrical properties of $\text{LBaMn}_2\text{O}_{6-x}$ ($L = \text{Pr}, \text{Nd}, \text{Sm}, \text{Eu}, \text{Gd}, \text{Tb}$) manganites, *Phys. Rev. B* **66**, 184424 (2002).
- [10] J. Blasco, G. Subías, M. L. Sanjuán, J. L. García-Muñoz, F. Fauth, and J. García, Structure and phase transitions in A -site ordered RBaMn_2O_6 ($R = \text{Pr}, \text{Nd}$) perovskites with a polar ground state, *Phys. Rev. B* **103**, 064105 (2021).
- [11] J. Blasco, G. Subías, J. L. García-Muñoz, F. Fauth, M. C. Sánchez, and J. García, Symmetry mode analysis of distorted polar/nonpolar structures in A -site ordered $\text{SmBaMn}_2\text{O}_6$ perovskite, *Phys. Rev. B* **103**, 214110 (2021).
- [12] J. Blasco, G. Subías, J. L. García-Muñoz, F. Fauth, and J. García, Determination of the crystal structures in the A -site-ordered YBaMn_2O_6 perovskite, *J. Phys. Chem. C* **125**, 19467 (2021).
- [13] T. Nakajima, H. Kageyama, and Y. Ueda, Dramatic change of magnetic property in the A -site ordered/disordered manganites $\text{PrBaMn}_2\text{O}_6/\text{Pr}_{0.5}\text{Ba}_{0.5}\text{MnO}_3$, *J. Magn. Magn. Mater.* **272–276**, 405 (2004).
- [14] T. Nakajima, H. Kageyama, and Y. Ueda, Successive phase transitions in a metal-ordered manganite perovskite YBaMn_2O_6 , *J. Phys. Chem. Solids* **63**, 913 (2022).
- [15] K. Yamauchi, Theoretical prediction of multiferroicity in $\text{SmBaMn}_2\text{O}_6$, *J. Phys. Soc. Jpn.* **82**, 043702 (2013).
- [16] D. Khomskii, Classifying multiferroics: Mechanisms and effects, *Phys.* **2**, 20 (2009).
- [17] Y. Ueda and T. Nakajima, Novel structures and electromagnetic properties of the A -site-ordered/disordered manganites $\text{RBaMn}_2\text{O}_6/\text{R}_{0.5}\text{B}_{0.5}\text{MnO}_3$ ($R = \text{Y}$ and rare earth elements), *J. Phys.: Condens. Matter* **16**, S573 (2004).
- [18] T. Nakajima, H. Yoshizawa, and Y. Ueda, A -site randomness effect on structural and physical properties of Ba-based perovskite manganites, *J. Phys. Soc. Jpn.* **73**, 2283 (2004).
- [19] N. Sicon, B. Ravel, Y. Yacoby, E. A. Stern, F. Dogan, and J. J. Rehr, Nature of the ferroelectric phase transition in PbTiO_3 , *Phys. Rev. B* **50**, 13168 (1994).
- [20] S. Lafuerza, J. García, G. Subías, J. Blasco, and V. Cuartero, Strong local lattice instability in hexagonal ferrites RFe_2O_4 ($R = \text{Lu}, \text{Y}, \text{Yb}$) revealed by x-ray absorption spectroscopy, *Phys. Rev. B* **89**, 045129 (2014).
- [21] See Supplemental Material at <http://link.aps.org/supplemental/10.1103/PhysRevB.107.165133> for the magnetoelectric phase diagram of A -site ordered RBaMn_2O_6 and A -site disordered $\text{R}_{0.5}\text{Ba}_{0.5}\text{MnO}_3$ perovskites studied in this investigation; a comparison between the x-ray-diffraction patterns of the ordered RBaMn_2O_6 and disordered $\text{R}_{0.5}\text{Ba}_{0.5}\text{MnO}_3$ ($R = \text{Sm}$ and Y) samples at room temperature; details about the experimental procedure to obtain k -range extended EXAFS free of Nd and Sm self-absorption and the comparison between the XANES spectra at the Mn K edge measured by high-energy resolution fluorescence detected (HERFD) and conventional core-hole lifetime broadened transmission modes.
- [22] K. Momma and F. Izumi, VESTA 3 for three-dimensional visualization of crystal, volumetric and morphology data, *J. Appl. Crystallogr.* **44**, 1272 (2011).
- [23] L. Simonelli, C. Marini, W. Olszewski, M. Ávila Pérez, N. Ramanan, G. Guilera, V. Cuartero, and K. Klementiev, CLÆSS: The hard X-ray absorption beamline of the ALBA CELLS synchrotron, *Cogent Phys.* **3**, 1231987 (2016).

- [24] L. Simonelli, C. Marini, L. Ribo, R. Homs, J. Avila, D. Heinis, I. Preda, and K. Klementiev, The CLEAR X-ray emission spectrometer available at the CLAES beamline of ALBA synchrotron, *J. Synchrotron Radiat.* **30**, 235 (2023).
- [25] S. Lafuerza, J. García, G. Subías, J. Blasco, and P. Glatzel, High-resolution Mn K-edge x-ray emission and absorption spectroscopy study of the electronic and local structure of the three different phases in $\text{Nd}_{0.5}\text{Sr}_{0.5}\text{MnO}_3$, *Phys. Rev. B* **93**, 205108 (2016).
- [26] S. Lafuerza, M. Retegan, B. Detlefs, R. Chatterjee, V. Yachandra, J. Yano, and P. Glatzel, New reflections on hard X-ray photon-in/photon-out spectroscopy, *Nanoscale* **12**, 16270 (2020).
- [27] M. Bianchini and P. Glatzel, A tool to plan photon-in/photon-out experiments: count rates, dips and self-absorption, *J. Synchrotron Radiat.* **19**, 911 (2012).
- [28] B. Ravel and M. Newville, ATHENA, ARTEMIS, HEPHAESTUS: Data analysis for X-ray absorption spectroscopy using IFEFFIT, *J. Synchrotron Radiat.* **12**, 537 (2005).
- [29] T. Nakajima, H. Kageyama, H. Yoshizawa, K. Ohoyama, and Y. Ueda, Ground state properties of the A-site ordered manganites, RBaMn_2O_6 ($R = \text{La}, \text{Pr}$ and Nd), *J. Phys. Soc. Jpn.* **72**, 3237 (2003).
- [30] S. V. Trukhanov, A. V. Trukhanov, H. Szymczak, R. Szymczak, and M. Baran, Thermal stability of A-site ordered $\text{PrBaMn}_2\text{O}_6$ manganites, *J. Phys. Chem. Solids* **67**, 675 (2006).
- [31] S. Yamada, Y. Maeda, and T. Arima, Successive electronic transitions and anisotropic properties in a double-perovskite $\text{SmBaMn}_2\text{O}_6$ single crystal, *J. Phys. Soc. Jpn.* **81**, 113711 (2012).
- [32] G. Qing-Qing, L. Jing-Bo, L. Guan-Nan, R. Guang-Hui, L. Jun, L. Guang-Yao, and L. Jing-Kui, Spin glass behavior in A-site ordered YBaMn_2O_6 compound, *J. Appl. Phys.* **114**, 053901 (2013).
- [33] D. Akahoshi, M. Uchida, Y. Tomioka, T. Arima, Y. Matsui, and Y. Tokura, Random Potential Effect near the Bicritical Region in Perovskite Manganites as Revealed by Comparison with the Ordered Perovskite Analogs, *Phys. Rev. Lett.* **90**, 177203 (2003).
- [34] J. J. Rehr and R. C. Albers, Theoretical approaches to x-ray absorption fine structure, *Rev. Mod. Phys.* **72**, 621 (2000).
- [35] P. Fornasini and R. Grisenti, On EXAFS Debye-Waller factor and recent advances, *J. Synchrotron Radiat.* **22**, 1242 (2015).
- [36] G. Subías, J. García, J. Blasco, M. C. Sánchez, and M. G. Proietti, Mn local structure effects in charge-ordered mixed-valence $\text{RE}_{1-x}\text{Ca}_x\text{MnO}_3$ (RE: La, Tb) perovskites: A review of the experimental situation, *J. Phys.: Condens. Matter* **14**, 5017 (2002).
- [37] T. J. Sato, J. W. Lynn, and B. Dabrowski, Disorder-Induced Polaron Formation in the Magnetoresistive Perovskite $\text{La}_{0.54}\text{Ba}_{0.46}\text{MnO}_3$, *Phys. Rev. Lett.* **93**, 267204 (2004).
- [38] J. Paras and A. Allanore, Contribution of electronic entropy to the order-disorder transition of Cu_3Au , *Phys. Rev. Res.* **3**, 023239 (2021).
- [39] D. Sedmidubský, A. Strejc, O. Benes, K. Kuzicka, J. Hejtmánek, P. Javorský, M. Nevřiva, and C. Martin, Energetics of charge order transition in $\text{Bi}_{1-x}\text{Sr}_x\text{MnO}_3$, *J. Solid State Chem.* **179**, 3798 (2006).
- [40] P. M. Woodward and P. Karen, Mixed valence in YBaFe_2O_5 , *Inorg. Chem.* **42**, 1121 (2003).
- [41] K. Hämäläinen, D. P. Siddons, J. B. Hastings, and L. E. Berman, Elimination of the Inner-Shell Lifetime Broadening in X-Ray Absorption Spectroscopy, *Phys. Rev. Lett.* **67**, 2850 (1991).
- [42] J. García, G. Subías, and J. Blasco, in *X-ray Absorption and Emission Spectroscopy: Theory and Applications*, edited by J. A. Van Bokhoven and C. Lamberti (John Wiley & Sons Ltd., 2016), Vol. 2, p. 459.